CHALMERS

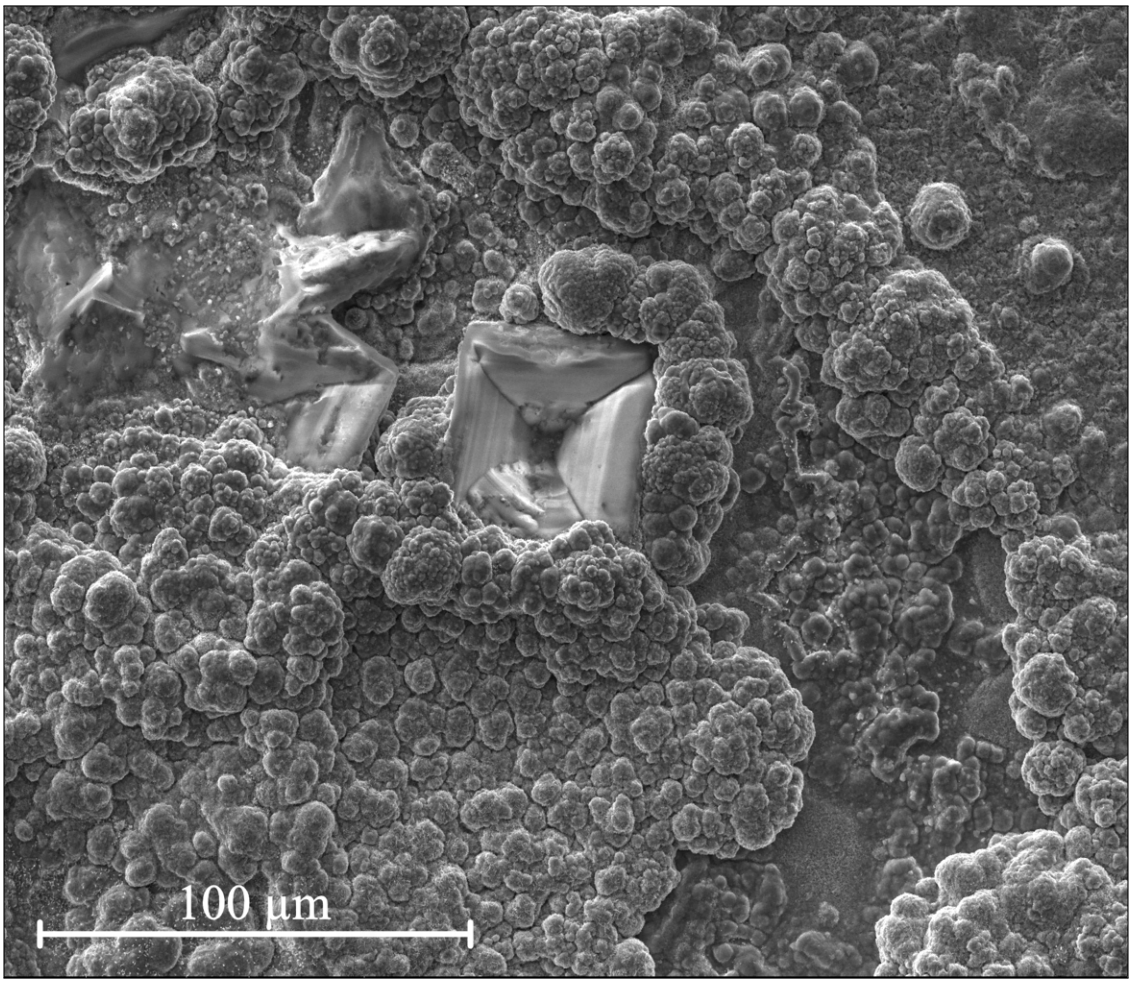

Investigating the corrosive effect of KCl on the low alloyed steel T22 at 400 °C

Bachelor´s thesis in Chemical Engineering

JONATHAN WARVNE

DEPARTMENT OF CHEMISTRY AND CHEMICAL ENGINEERING
CHALMERS UNIVERSITY OF TECHNOLOGY
Gothenburg, Sweden 2022
www.chalmers.se

Bachelor's thesis 2022

Investigating the corrosive effect of KCl on the low alloyed steel T22 at 400°C

JONATHAN WARVNE

CHALMERS

Department of Chemistry and Chemical Engineering
Division of Energy and Materials
Chalmers University of Technology
Gothenburg, Sweden 2022

Investigating the Corrosive Effect of KCl on the Low Alloyed Steel T22 at 400°C
JONATHAN WARVNE

Supervisor: Hampus Lindmark, PhD student, Department of Chemistry and Chemical Engineering
Examiner: Jesper Liske, Associate Professor, Department of Chemistry and Chemical Engineering

Bachelor's Thesis 2022
Department of Chemistry and Chemical Engineering
Division of Energy and Materials
Chalmers University of Technology
SE-412 96 Gothenburg
Telephone +46 735 099 460

Cover: Surface morphology of T22 steel exposed to $0.1 mg/cm^2$ KCl for 24h at 400°C. Image taken using SEM operating with a secondary electron detector at an accelerating voltage of 15kV.

Gothenburg, Sweden 2022

Investigating the Corrosive Effect of KCl on the Low Alloyed Steel T22 at 400°C
JONATHAN WARVNE
Department of Chemistry and Chemical Engineering
Chalmers University of Technology

Abstract

Substituting fossil-fuels with waste- and biomass during combustion for heat-and power production has proven to be a viable, more environmentally friendly energy source. It does however come with new problems, one being the release of a diverse flue gas containing different chlorine species such as KCl, HCl and $PbCl_2$ which are known to greatly accelerate the corrosion of low-alloyed steels commonly used in the waterwall region of waste-fired boilers. To solve this problem a better understanding of the corrosive mechanisms at play during chlorine-assisted corrosion of low alloyed steels at high temperatures is required. This thesis aims to investigate the corrosive effect of KCl on the low-alloyed steel T22 at 400°C through the use of several analytical techniques such as SEM, EDX and XRD. The results reveal that KCl greatly increases the magnitude of corrosion under these conditions as can be seen by both mass-gain data, SEM images and by the extensive crack formation found on salt affected samples after 168h of exposure. XRD-data confirmed the formation of Hematite(Fe2O3) and Magnetite(Fe3O4) on nearly all samples. EDX results indicate that Cl can diffuse through the oxide scale and reach the metal interface where it is proposed to form volatile metal-chlorides according to the chlorine cycle mechanism.

Keywords: High-temperature corrosion, Low-alloyed steel, Chlorine-induced corrosion, KCl, HTC

Acknowledgements

First and foremost i would like to thank my supervisor, Hampus Lindmark, for providing guidance and support throughout the project and for stepping in and taking an active role in various practical moments when things didn´t go according to plan. I would also like to thank my examiner, Jesper Liske, without whom this project wouldn´t have been possible. Lastly i would like to thank the members of the high temperature corrosion centre at Chalmers, both for being very welcoming and for providing assistance in various ways throughout the project.

Jonathan Warvne, Gothenburg, June 2022

List of Acronyms

HTC	High-Temperature Corrosion
BIB	Broad Ion Beam
SEM	Scanning Electron Microscopy
EDX	Energy Dispersive X-ray
XRD	X-ray Diffraction
SE	Secondary Electron
BSE	Back-scattered Electron

Contents

1 | Introduction

As the global dependency on fossil fuels persists there is a large push to adopt more climate-friendly and renewable energy sources. While energy sources such as wind, water and solar energy are great alternatives they are highly dependent on geographic factors and thus not always a reliable option. An area that holds a large potential is the substitution of fossil fuels with waste and biomass during combustion for heat and power generation. This includes the use of everything from industrial waste to wooden by-products and can therefore be utilized wherever such a supply exists. In a country like Sweden with a readily available supply of biomass from its forest industry this type of combustion is a highly viable alternative and has become the preferred fuel in combined heat- and power production plants. [1].

Combustion of biomass can, however, lead to new complications during the combustion process. Biomass by nature is very heterogenous and, during combustion, will release a wide variety of byproducts. The flue-gas that is formed during combustion can contain, among other things, various chlorine species such as KCl, HCl and $PbCl_2$ which are known to seriously increase the corrosion rate of metal components in a waste-fired boiler [2–4]. One of the areas susceptible to corrosion in this environment is the waterwall-region in the boiler furnace [5, 6]. The waterwalls are comprised of steel tubes designed to separate the water inside from the flue-gas outside. Low-alloyed steels are commonly used for this purpose due to a good balance between mechanical properties and low material cost. However, the harsh environment on the furnace-side in addition to the high working temperatures will expose the tube wall to high-temperature corrosion which will lead to material loss and, in time, corrosive breakdown of the material. This environment places a high demand on the anti-corrosive properties of the material. Common countermeasures against high-temperature corrosion include using stainless steels, Aluminum- or Nickel- based alloys, coating the metal with thermal coatings or pre-treating the biomass before combustion to reduce the concentration of contaminants. [3]. While these methods provide good anti-corrosive results, they come with a significant increase in cost. Another option to mitigate the corrosive effect of the materials is to reduce the operating temperature during combustion. However, this will have a negative effect on the electrical efficiency of the fuel to energy conversion process as the steam parameters will be reduced.

Neither of these options are desirable from an economic standpoint and as such

there is a large incentive to investigate and fully understand the high-temperature corrosion mechanisms at play in the presence of alkali chlorides on commonly used steels in order to find a viable, cost-effective way to mitigate the corrosion of the waterwall material and to prevent premature failure in water wall applications.

1.1 Purpose

This report aims to investigate the corrosive effect of KCl on the low alloyed steel T22 in a controlled lab-environment designed to simulate that of the waterwall-region in an industrial waste-fired boiler.

1.2 Limitations

Studying the kinetics of oxide scale formation during high-temperature corrosion is often of great interest and importance in real-world applications. However, due to time and equipment considerations an in-depth study of the kinetics of oxidation will not be undertaken and the report will instead focus on investigating corrosion and oxide morphology through visual analysis using techniques such as SEM, EDX and XRD.

2 | Theory

Corrosion, the dissolution of a metal into a more chemically stable oxide, occurs naturally as a metal is exposed to oxygen containing environment [7].The degradation of the metal by its environment is usually electrochemical in nature and involves an oxidizing agent, usually dissolved oxygen or hydrogen cations, and an electrolyte where charged species can travel. Since it is an electrochemical reaction it can be described in terms of two half cell reactions: a cathodic reaction and an anodic reaction [7].

$$\mathit{Anodic\ reaction} : \mathrm{M(s)} \longrightarrow \mathrm{M(aq)}^{2+} + 2\,\mathrm{e}^- \tag{2.1}$$

$$\mathit{Cathodic\ reaction} : O_2(g) + 2H_2O(l) + 4e^- \longrightarrow 4\,\mathrm{OH}^- + \mathrm{H}_2 \tag{2.2}$$

Equation 2.1 is an example of the anodic oxidation of a generic metal while eq 2.2 shows a cathodic reduction where oxygen acts as the oxidizing agent. An important criteria for a corrosion reaction that is fulfilled by the anodic reaction is the simultaneous transfer of both mass and charge across the metal/electrolyte interface which is what ultimately makes the metal corrode and leads to a mass loss of the material [7]. While this type of corrosion is the most widespread and commonly occurring it is also possible for a metal to corrode in the absence of an electrolyte, especially given high enough temperatures [7–9].

2.1 High-Temperature Corrosion, HTC

High-temperature oxidation and subsequent corrosion can occur when a metal is exposed to a gaseous oxidizing agent, usually oxygen, at high temperatures [7–9]. This phenomenon is not as widespread as aqueous corrosion and mainly occurs in industrial high-temperature environments such as power-plants, gas turbines, engines or industrial boilers [8].

2.1.1 Distinction Between HTC and Aqueous Corrosion

While aqueous corrosion and high-temperature corrosion transpire in different conditions the governing principle behind both phenomenona stay the same: Coupled oxidation and reduction reactions. [7]

$$Oxidation : \mathrm{M(s)} \longrightarrow \mathrm{M(s)}^{2+} + 2\,\mathrm{e}^- \tag{2.3}$$

$$Reduction : \frac{1}{2}\,\mathrm{O_2(g)} + 2\,\mathrm{e}^- \longrightarrow \mathrm{O}^{2-}\mathrm{(g)} \tag{2.4}$$

$$Overall\ reaction : \mathrm{M(s)} + \frac{1}{2}\,\mathrm{O_2(g)} \longrightarrow \mathrm{MO(s)} \tag{2.5}$$

Equations 2.3-5 are examples of generic oxide formation reactions where the electrons produced by the oxidation of the metal are consumed in the coupled reduction of oxygen. This reaction takes place on the metal surface [7].

Aqueous corrosion is quantified by a loss of material as the metal is oxidized and dissolved in solution [7]. HTC is instead characterised by the formation of an oxide scale on the metal surface and is in many cases quantified by an associated increase in mass as the corrosion product grows in thickness. The type of oxide formed depends on the metal and its alloying elements. It has the potential to protect the metal from further corrosion by acting as a barrier between the metal and the oxidizing agent, hindering diffusion between the two. Some important properties of the oxide scale are thickness, growth direction and mechanical properties [7, 8].

Studying the behavior and properties of the oxide scale is therefore integral to understanding and preventing high-temperature corrosion.

2.1.2 Thermodynamics of High-Temperature Corrosion

As previously stated, corrosion is a naturally occurring phenomenon and even tough sufficiently high-temperature environments may not be found naturally the governing principle remains the same. In the presence of an oxidizing agent a metal will undergo oxidation to form a more thermodynamically stable oxide [8, 9]. As with all reactions, oxide formation comes with an associated change in free energy and many such reactions have a very negative ΔG meaning they are spontaneous. This is especially true at high temperatures. The change in free energy associated with the formation of different oxides can be represented as a function of temperature and partial pressure of oxygen in an Ellingham diagram [7–9].

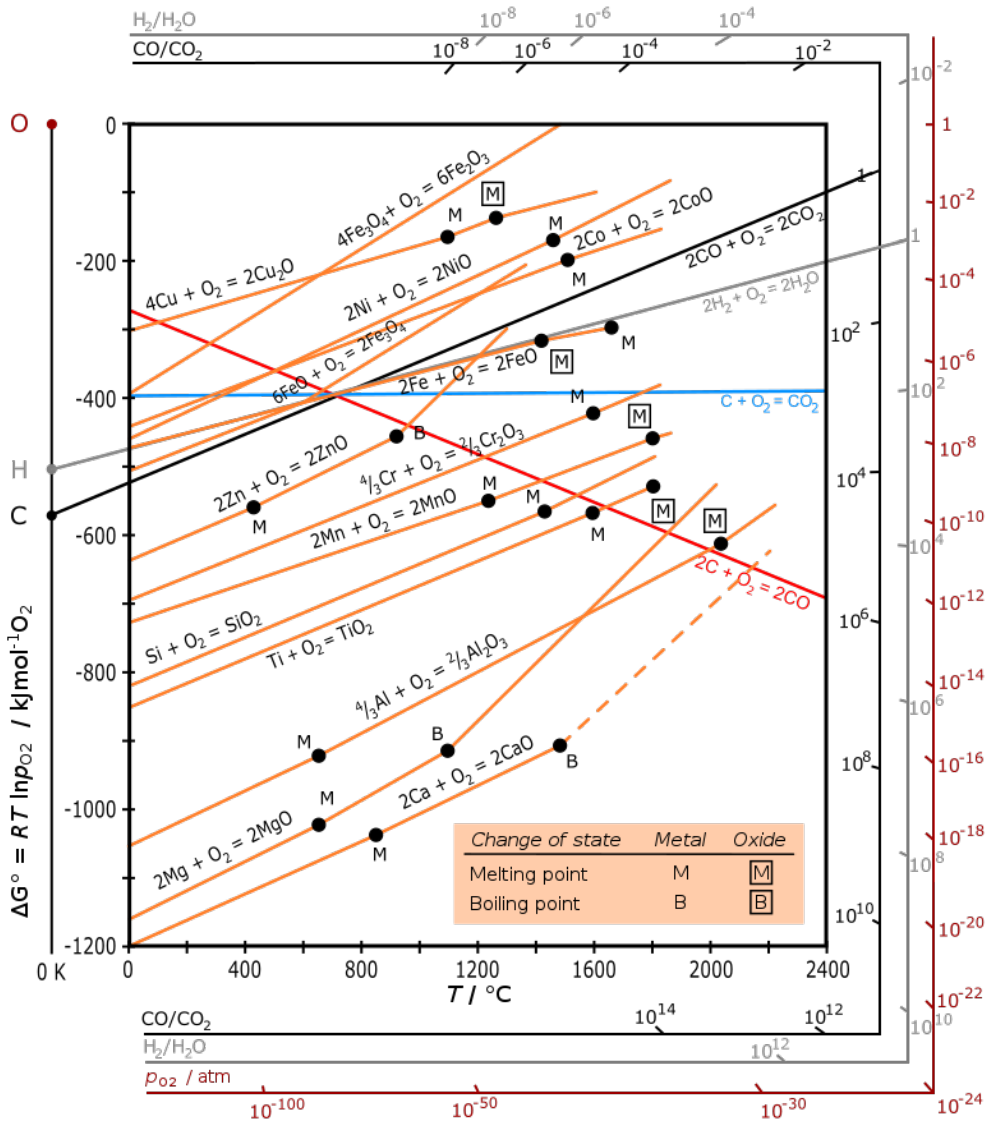

Figure 2.1: In the Ellingham diagram the equilibrium between metal and oxide is illustrated. Lines represent equilibrium between metal and oxide. Slope of lines related to changes in entropy. As the system becomes more ordered (less gaseous products) the entropy decreases resulting in a positive slope. [10]

The lines in the Ellingham diagram represent equilibrium between oxide and metal where the positive slope represents the standard entropy change for the oxidation reaction. While above a certain equilibrium line the oxide is the more stable product while underneath it the metal is stable. The difference in driving force to form different oxides is significant and greatly affects oxidation of alloys with multiple oxide-forming elements. Stainless steels for example can form Chromia (Cr_2O_3) as well as iron oxides such as Hematite (Fe_2O_3) and Magnetite (Fe_3O_4) but since the driving force to form Chromia is much greater this becomes the primary oxide and the first to form [7–9].

2.1.3 Oxide growth: Mechanism and Growth Direction

Initiation of oxide formation occurs on the metal surface when O_2 adsorbs on the metal surface and eventually dissolves into the metal at which point the corrosion product can nucleate and begin growing laterally across the surface [7, 8]. As the surface becomes covered in a homogenous layer growth continues outward through ion and electron diffusion in the scale. This is also illustrated in equations 2.3 and 2.4. Metal cations and electrons are needed at the oxide/gas interface to continue the corrosion process. As seen in figure 2.2 both ionic and electronic conductivity is required to facilitate continued oxide growth [7].

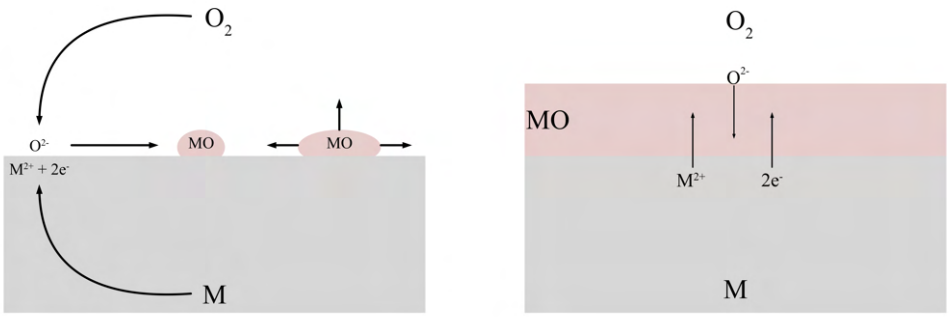

Figure 2.2: Illustration of ion diffusion during oxidation. When an oxide layer has formed diffusion of ions through it is necessary for further growth [7].

2.1.3.1 Diffusion through Defects in Oxide Microstructure

To predict the growth of the oxide scale an understanding of the diffusion mechanism in the oxide is necessary. Even though the oxide does not share the crystalline microstructure of its parent alloy it still contains defects which enable diffusion of ionic species through the material. Two types of defects are critical for ion mobility in the oxide scale: Point defects due to ion vacancies(ion deficit) or interstitial ions(ion excess) [7, 8]. Both of these defect types are depicted in figure 2.3. While these point-defects are the most important in determining the properties of the oxide scale.

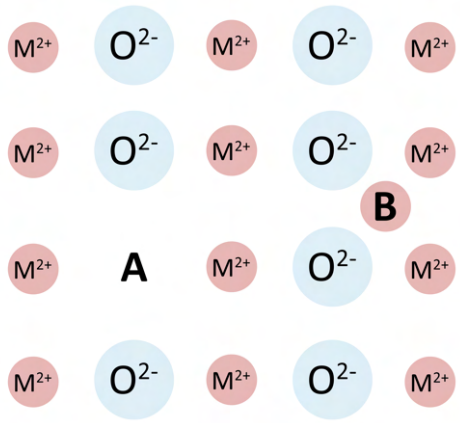

Figure 2.3: Important defects for ion diffusion in oxides. Point A is an example of a vacant anion while point B shows an interstitial cation. [7, 8]

Diffusion through vacancies occur when a nearby ion moves into a vacant spot and leaves a new vacancy in its wake for another ion to move into. This process continues throughout the material. The mechanism is similar for interstitial movement. Figure 2.4 shows a visual representation of ion movement [7].

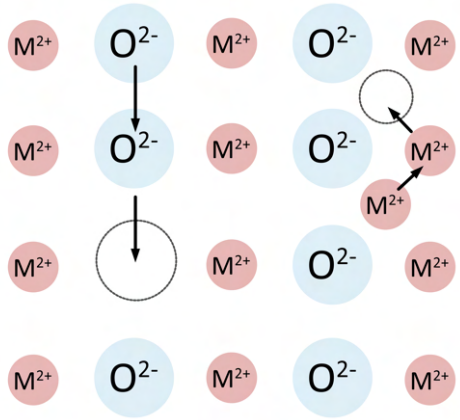

Figure 2.4: Mechanisms of ion diffusion through the oxide due to anion vacancy or interstitial cations. [7].

As a consequence of having an excess or deficit in ions the oxide will attain either a net positive or a net negative charge which will require electrons from the metal substrate to achieve a neutral charge. This enables electronic diffusion through the oxide which gives it semiconductor properties [8].The predominant defect type in the oxide scale will have a large impact on the growth behaviour of the oxide and it is common to categorize oxides by their defects. The two types are n-type and

p-type semiconductors. These oxides and their defects are summarized in table 2.1. This classification is made for oxides that are non-stoichiometric. These are oxides with a high concentration of defects, often due to different possible oxidation states of the parent metal, meaning they deviate from their stoichiometric formula due to an excess or deficit of ions. Iron with it´s different oxidation states will create a non-stoichiometric iron oxide. Stoichiometric oxides, like Al_2O_3, on the other hand have a low concentration of defects [8].

Table 2.1: Classes of non-stoichiometric oxides and their predominant defect types. Anions are not commonly found in interstitial positions due to their size.

Oxide Classification	Predominant Defect
N-type Semiconductor	Anion Vacancies, Interstitial Cations
P-type Semiconductor	Cation Vacancies, Interstitial Anions(uncommon)

Since cations are sourced from the metal substrate cation diffusion due to cation vacancies or interstitial cations will only ever occur outward leading to oxide scale growth at the scale/gas interface [8]. Anion diffusion in the same manner will cause scale growth at the metal/scale interface which can facilitate internal oxidation where the oxide grows into the material. The consequences for this can be devastating as the mechanical properties of the metal can deteriorate. Factors that greatly affect the diffusion process are temperature and the presence of grain boundaries which act as short-cuts for diffusion [8]. The diffusion process is highly temperature dependant and can be described using the Arrhenius equation [8]:

$$D(T) = D_0 exp(-\frac{\Delta H}{RT}) \tag{2.6}$$

In equation 2.6 D is the diffusion coefficient, D_0 is the frequency factor, R is the as constant, T is the temperature and ΔH is the activation enthalpy of diffusion [8].

2.1.3.2 Criteria for a Protective Oxide

Many factors affect how well an oxide can protect the underlying metal from corrosion. An oxide can be considered protective if it fulfills the following criteria [9]:

- Continuous across the metal surface: A homogenous layer across the surface of the metal ensures good protection.
- Well adherent to the metal surface: The oxide must not spall of or crack due to differences in thermal expansion.
- Thin and slow-growing : A fast growing oxide is indicative of a high rate of diffusion between the metal and the gas.

- Higher melting point than underlying metal.
- Not volatile in high-temperature environment.

The protective properties of oxide scales are largely determined by the scale microstructure. As mentioned above the driving force for continued oxide growth is diffusion of ions and electrons through the scale to fuel the oxide forming reactions(eq. 2.3-5). It follows then that a large diffusion potential through the scale results in a non-protective oxide and since diffusion is governed by defects in the microstructure a higher concentration of defects leads to a higher rate of diffusion and, consequently, diminished protection against HTC.

2.1.3.3 Common Oxides and their Parent Alloys

There exists an established hierarchy of protective oxides where iron oxides formed by low-alloyed steels typically display poor protective properties at higher temperatures and stainless steels or Al-based alloys perform better [9]. Some common alloys and their respective oxides are listed in table 2.2.

Table 2.2: Common alloys and their corresponding oxides [9].

Parent Alloy	Predominant Oxide	Temperature limit
Low-alloyed steels, <10% Cr content	FeO,Fe_2O_3,Fe_3O_4	Up to 500°C
Stainless steels, >10% Cr content	Cr_2O_3	Up to 650°C
Stainless steels with addition of Nickel	Cr_2O_3	Up to 850°C
Fe-Cr-Al Alloys	Al_2O_3	Up to 1100°C

As detailed in table 2.2 low-alloyed steels are commonly defined as steels with a Cr-content lower than 10%. This amount prevents the metal from forming a protective Chromia(Cr_2O_3) scale and forces it to rely on lesser iron oxides for protection. The same principle holds true for other alloying elements where certain amount is needed to facilitate the formation of a particular oxide. What makes oxides like Al_2O_3 and Cr_2O_3 protective are their lower defect concentration. Stainless steels and Fe-Cr-Al alloys will, during initial corrosion stages, form a thin oxide layer impervious to further diffusion. This layer provides great protection for the metal until damaged by external factors(scratches, extreme environments) [9].

2.1.4 A Note on Corrosion Kinetics

As previously stated the kinetics of corrosion will not be studied due to time and equipment constraints. It is, however, of interest to briefly introduce the role of kinetics during high-temperature corrosion.

As with diffusion the overall kinetics of corrosion can be described using Arrhenius equation when considering a general oxide formation reaction like eq.2.5. [7, 8]:

$$k = A'exp(-\frac{\Delta E_a}{RT}) \tag{2.7}$$

In equation 2.7 k is the reaction rate constant, A' an exponential factor,ΔE_a the activation energy for the reaction and R and T the gas constant and temperature respectively [7]. The kinetics of high-temperature oxidation can be described by three different rate laws, each of which describe different rate-limiting steps during oxide formation [7].

- Linear Rate Law: Reaction rate is constant at the metal/oxide interface. Oxidizing agent has easy access to the metal substrate through cracks or pores. Indicates the lack of a protective oxide.

- Parabolic Rate Law: Diffusion of ions or electrons through oxide is rate-limiting. High initial corrosion rate that tapers off when a protective oxide has formed.

- Logarithmic Rate Law: Can describe kinetics of very thin films or oxidation at lower temperatures. Also valid during initial corrosion stages.

In figure 2.5 the different rate laws are represented by plotting mass gain as a function of time.

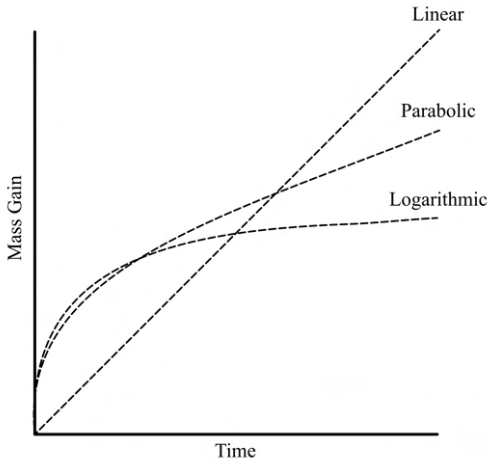

Figure 2.5: Theoretical rate laws governing the corrosion rate during HTC.

In practice corrosion rates will only follow these curves loosely and differ depending on oxide protection. If an oxide breaks down due to external factors such as scratches a sharp increase in mass gain will be recorded. This is called breakaway-oxidation. If the oxide can re-form a lower rate of mass gain will once again be seen [7].

2.1.5 Predicting the Behaviour of T22 in the Presence of Salt

Since T22 is a low alloyed steel with an insufficient amount of Cr to form a protective Cr_2O_3 layer it will instead form different iron oxides. FeO,Fe_2O_3 and Fe_3O_4 may form during different stages during corrosion and neither will provide good protection against further oxidation. The iron oxides will, however, provide some resistance against diffusion and as such the corrosion rate of the metal will see an initial linear increase and then loosely follow the parabolic behaviour described in section 2.1.4.

The effect of alkali-chlorides on high-temperature corrosion is well a documented in HTC reasearch [11–21]. The aggressive atmosphere can break down the protection of otherwise protective oxides. There are two proposed mechanism behind the chlorine-assisted corrosion of low-alloyed steels: The chlorine-cycle, or active oxidation, and a electrochemical coeeosion mechanism [11, 19].

2.1.5.1 The Chlorine-cycle

The chlorine-cycle is initiated by formation of gaseous molecular chlorine, Cl_2, through oxidation of KCl or a reaction between KCl and the oxide scale according to equation 2.8 [11, 19]:

$$2\,\mathrm{KCl(s)} + \mathrm{Fe_2O_3(s)} + \frac{1}{2}\,\mathrm{O_2(g)} \longrightarrow \mathrm{K_2Fe_2O_4(s)} + \mathrm{Cl_2(g)} \tag{2.8}$$

Cl_2 proceeds to diffuse through the grain boundaries of the oxide scale. Upon reaching the metal/oxide interface metal and chlorine reacts to form volatile metal chlorides according to reaction 2.9 [11, 19]:

$$\mathrm{M(s)} + \mathrm{Cl_2(g)} \longrightarrow \mathrm{MCl_2(g)} \tag{2.9}$$

Due to a lower partial pressure of oxygen on the inner part of the oxide scale the volatile compound will diffuse outward and become oxidized as the partial pressure increases as shown in reaction 2.10 [11, 19].

$$2\,\mathrm{MCl_2(g)} + \frac{3}{2}\,\mathrm{O_2(g)} \longrightarrow \mathrm{M_2O_3(s)} + 2\,\mathrm{Cl_2(g)} \tag{2.10}$$

The Cl_2 is then proposed to recirculate back down to the metal to continue the cycle or be released into the atmosphere. The chlorine-cycle theory is not fully accepted due to the unknown diffusion mechanism of Cl_2 through the oxide. If Cl_2 can diffuse through cracks or pores in the scale O_2 should also be able to diffuse due to it´s smaller size. This would lead to a higher oxygen partial pressure on the inside of the scale and drastically change both oxide formation and the theoretical metal chloride

formation. However the presence of metal chlorides under the oxide would support the theory. The chlorine-cycle is illustrated in figure 2.6 [11, 19].

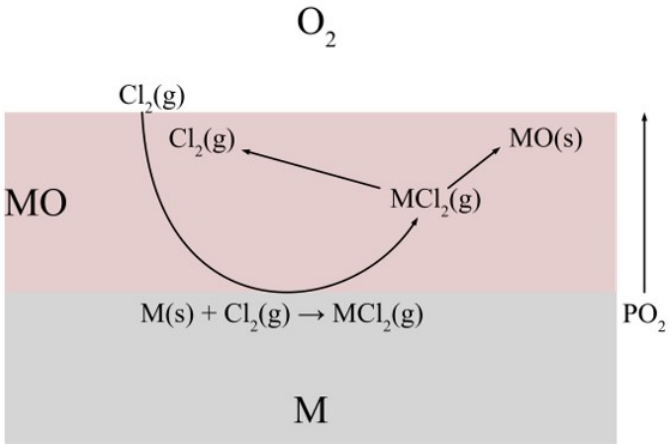

Figure 2.6: Chlorine cycle in a generic metal/oxide: M/MO. [11]

.

2.1.5.2 Electrochemical Corrosion Mechanism

The theory of the electrochemical corrosion mechanism is similar but provides an alternate explanation for the problematic Cl_2 diffusion. The mechanism proposes ionic and electronic diffusion as the driving force in place of Cl_2 diffusion. Here Cl_2 is reduced with the electrons provided by the metal oxidation reaction [11, 19].

$$\mathrm{M(s)} \longrightarrow \mathrm{M^{2+}} + 2\,\mathrm{e^-} \tag{2.11}$$

$$\mathrm{Cl_2(g)} + 2\,\mathrm{e^-} \longrightarrow 2\,\mathrm{Cl^-(g)} \tag{2.12}$$

Cl^- is then proposed to migrate through grain boundaries, forming metal chlorides in its path [11, 19]. In the presence of KCl the formation of Cl^- may also occur according to equation 2.13.

$$2\,\mathrm{KCl(s)} + \mathrm{H_2O(g)} + \frac{1}{2}\,\mathrm{O_2(g)} + 2\,\mathrm{e^-} \longrightarrow 2\,\mathrm{KOH(g)} + 2\,\mathrm{Cl^-(ads)} \tag{2.13}$$

2.2 Scanning Electron Microscopy, SEM

Scanning electron microscopy is an analytical tool widely used in the field of material science due to its ability to image surfaces at a scale of down to 0.2µm with a high resolution [22]. This is accomplished by accelerating an electron beam towards the sample and capturing and analyzing the different signals emitted as the electrons of the beam and the sample interact. The electron beam is generated in an electron gun and accelerated towards the sample. The system is operated under vacuum to allow

electrons an path to the sample free of interference. Electrons have a interaction volume of a few micrometers and upon interaction with the sample atoms they will scatter in different ways and in so doing generate various signals, each providing different information. The most important of these signals secondary electrons, SE, backscattered electrons, BSE, and characteristic x-rays. Analyzing these signals allows for topographic and compositional information to be obtained. Figure 2.7 illustrates the origin of the different signals. BSE originate from the incident electron beam while SE and characteristic X-rays originate from the sample atom [22].

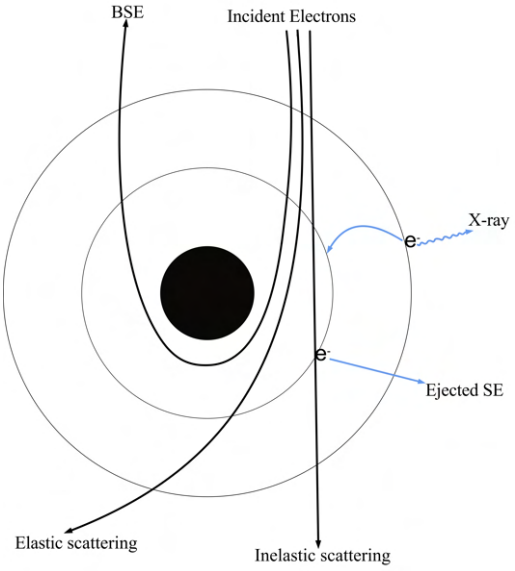

Figure 2.7: Illustration showing the origin of different signals obtained when scanning an electron beam over the sample surface [22].

2.2.1 Information From Back-scattered Electrons, BSE

Back-scattered electrons are the result of elastic scattering of incident electrons [22]. Elastic scattering occurs due to attractive forces between beam electrons and the positive nucleus of a sample atom. Electrons are scattered at different angles and backscattering of electrons can occur. A larger atom with a stronger postive charge will have a stronger interaction with beam electrons and provide a higher degree of elastic scattering. This gives BSE detectors the ability to provide some degree of compositional information by giving a contrast based on atomic weight, a lighter visual signal for heavy elements and a darker signal for lighter elements. This information alone is not enough quantify the composition of a sample but it is an useful tool to identify different phases and regions for further analysis. BSE retain a high kinetic energy and therefore have a high interaction volume [22].

2.2.2 Information From Secondary Electrons, SE

Secondary electrons are the result of inelastic scattering. Inelastic scattering occurs when a beam electron with sufficient energy collides with the electron of a sample

atom and knocks it out of orbit. Due to a lower kinetic energy of secondary electrons these are only ejected from the top nanometer layer of the sample resulting in a low interaction volume, enabling high resolution imaging when using a SE detector. During SE detection the contrast is a result of a variance in secondary electrons generated which is greatly impacted by surface geometry and orientation. A rough surface will have a high variance in SE signals which provides a highly contrasted image.

2.2.3 Difference in BSE and SE Imaging

Figure 2.8 shows the same area of a sample viewed in both SE and BSE mode:

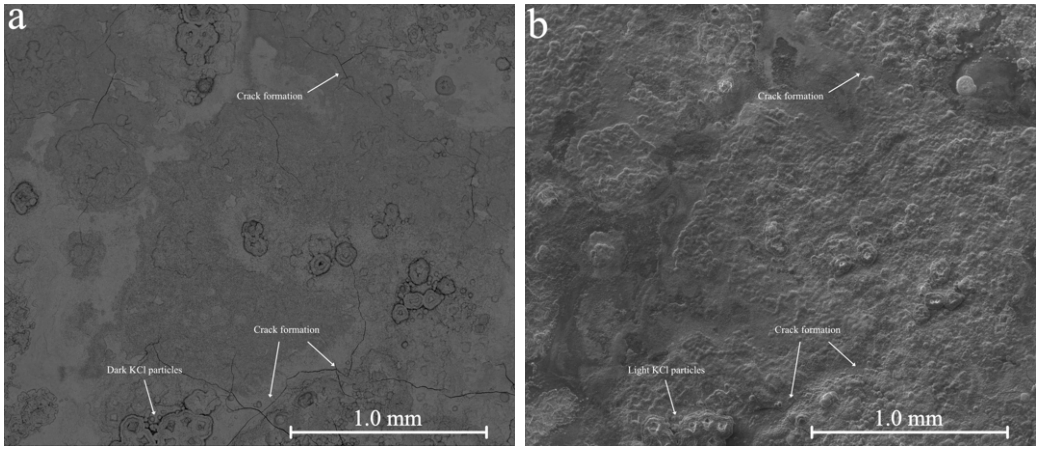

Figure 2.8: Surface overview of a sample exposed to KCl for 168h. Image 2.8a is taken in BSE mode and 2.8b in SE mode.

When observing the salt particles on the sample the difference in signal between the SE detector and the BSE detector are clear. Since KCl is lighter than Fe or its oxides it is displayed in a dark color in the BSE image. In the SE image the flat surface show little contrast while the rougher parts of the sample are heavily contrasted. The SE mode shows no discernible difference between the salt particle and the surrounding oxide. Cracks are easily discernible in BSE mode.

2.2.4 Energy Dispersive X-ray, EDX

When a secondary electron is knocked out of its shell a outer-shell electron with a higher energy level will relax down in an effort to minimize energy [22, 23]. This results in an energy difference that is released in the form of a characteristic x-ray. The characteristic x-rays released during the relaxation of outer shell electrons are unique for different atoms and can provide quantitative compositional information as a good complement to BSE imaging. An ED spectrometer for x-ray detection is often incorporated into the SEM instrument and provides a spectra of atomic signals and compositional information sorted by weight or molar ratio which is a useful tool to confirm the presence of elements or investigate elemental composition of unknown phases [23].

2.2.5 X-ray Diffraction, XRD

While EDX can be used to identify the elemental composition of a sample it cannot determine how these elements are arranged. To determine what compounds or phases are present on a sample XRD can be used. XRD works by probing a crystalline sample with an x-ray of known wavelength and measuring the waves that are diffracted from the crystal lattice of the surface [24]. The driving principle during XRD is the constructive interference between the diffracted waves and the crystal structure of the sample. X-rays are diffracted in different directions and constructive interference will occur at specific angles. This relation can be described using the Bragg equation [24].

$$n\lambda = 2dsin\Theta \tag{2.14}$$

Here λ is the reflection wavelength, n an integer, Θ the angle between crystal planes of the sample and the incident beam, also called the bragg angle, and d is the distance between planes in the crystal where the reflection occurs. By measuring the bragg angles and the intensities of the diffractions and comparing these to a reference database the presence of specific compounds can be determined. Due to the possibility of overlapping signals between different compounds it is important to know what elements are present on the surface before analysis. This makes EDX and XRD good complementary techniques. [24].

2.2.6 Broad Ion-Beam, BIB

Before analyzing sample cross-sections with SEM it is desirable to achieve a highly polished surface beyond that which can be achieved through mechanical polishing. Broad ion beam, BIB, can be used to polish surfaces by bombarding them with an ion beam to remove surface atoms as the incident-beam and sample atoms collide [25].The beam originates from ion-guns, often argon-based, and is accelerated towards a small exposed part of the sample. Upon collision with surface atoms of a sample an energy transfer occurs and atoms are released from the surface [25].

3 | Method and Materials

This section details the methodology and the instruments used during experiments. The project can be divided into two main parts: Exposure and analysis. Before each step necessary sample preparations must be made. Alongside these steps, a literary study will be conducted to provide a necessary frame of reference for analyzing and drawing conclusions around the results. The material used throughout the project is the low-alloyed steel T22. Its composition is detailed in the table 3.1.

Table 3.1: Composition of T22 in wt%

Cr	Mo	Mn	Si	C	P	S
1.9-2.6	0.87-1.13	0.3-0.6	<0.50	0.05-0.15	<0.025	<0.025

3.1 Preparation Before Exposure

Before exposure T22 steel coupons of dimensions 15x15x2 mm were prepared by grinding and polishing with silicon carbide paper with a grit size of 1000 for the edges and a grit size of 320 for the surface until they were homogenous and free of scratches. Furthermore the surface was polished using polishing discs with grain sizes from 9µm to 1µm together with a diamond suspension until a mirror-like surface was achieved. Coupons were degreased in acetone under ultrasonic agitation and stored in a desiccator. KCl was deposited on samples by spraying them with a solution of KCl in 80:20 ratio of ethanol and water. The high ethanol ratio ensures rapid evaporation and a homogenously distributed layer of salt. The coupons were measured and weighed before, and during spraying to achieve a deposition of 0.1 mg/cm^2 of surface area. The coupons were finally inserted into an furnace with a temperature of 400°C +- 1°C and a gas composition of 5% O_2, 20%H_2O and 75%N_2. The total gas flow in the furnace was 3 cm/s. Upon extraction from the furnace samples were left to cool and then weighed to determine mass change after exposure. A rough schematic of the furnace is depicted in figure 3.1.

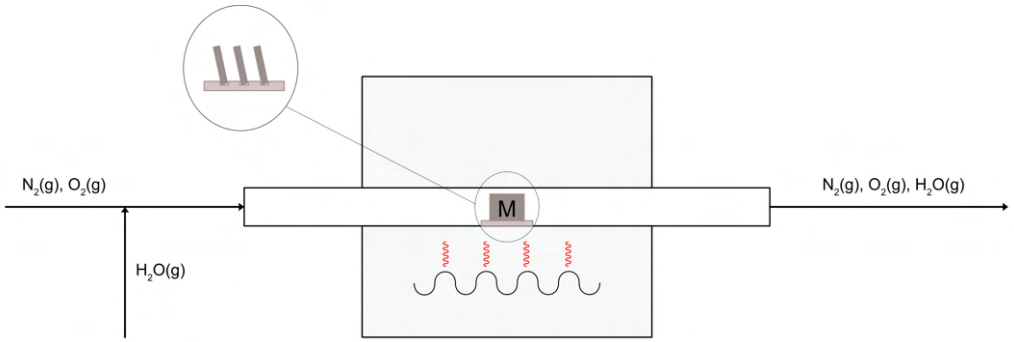

Figure 3.1: Schematic of furnace used during exposures. Samples are loaded on a ceramic tray and inserted into the furnace.

Exposures where performed for three different time intervals. 1h, 24h and 168h. For each interval three samples with salt deposited in addition to three reference samples were inserted into separate furnaces to avoid contamination of the reference samples.

3.2 Microstructure Analysis using SEM, EDX and XRD

Microstructure analyses were conducted using SEM, EDX and XRD instrument. The SEM and EDX analysis were performed on a FEI QUANTA 200 FEG ESEM instrument with an Oxford Inca energy dispersive X-ray (EDX) detector coupled to the SEM instrument. Both backscattered electrons (BSE) and secondary electrons (SE) detector were used and an accelerated electron voltage of 15-20 KeV were conducted.

Prior to cross sectional analysis the exposed samples were sputter coated with gold in order to increase the conductivity of the material and to increase the contrast on the sample. Subsequently a silicon wafer was glued on top of the sample using Loctite 415 and dried overnight. The samples were then cut using a Struers TXP instrument using 2100rpm. The cut cross section was then polished and subsequently refined using BIB with argon ions as sputtering element. The cross section was exposed in the BIB instrument for 6h using an accelerating voltage of 8kV and a current of 3mA.

XRD analysis was conducted to analyze the different oxide phases observed after the exposure. The XRD analysis was conducted on a D8 Discover instrument and the results were later matched with a database were different possible oxides that fit the peak pattern of the results were chosen.

4 | Results

In this section the experimental results are presented and analysis of selected samples are presented.

4.1 Effect of KCl on corrosion rate

As mentioned in section 2.1.1 the corrosion rate in high-temperature environments can in many cases be quantified by an increase in mass as the oxide scale is formed. Figure 4.1 illustrates the average mass gain from different exposures with and without salt.

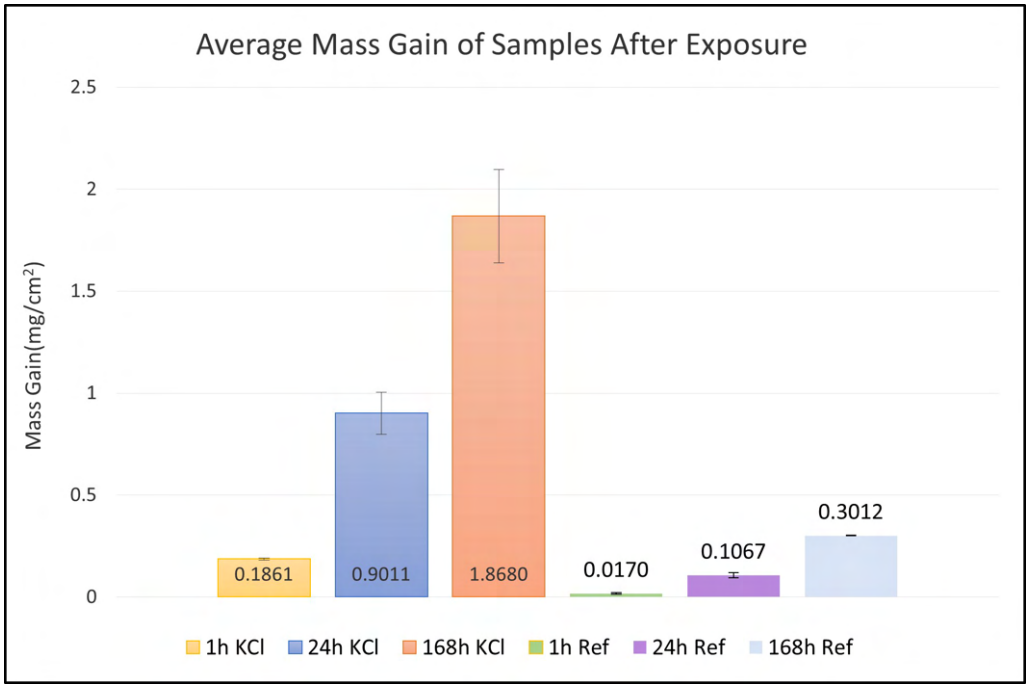

Figure 4.1: Average mass gain of samples with and without salt.

As expected the presence of KCl severely impacts the corrosion rate of the metal with 1h samples seeing an increase in mass gain by a factor of 10 and 24h samples by a factor of 8.4 when coated with salt. The mass gain of 0.11 mg/cm^2 for reference

samples and 0.90 mg/cm^2 for samples exposed to salt for 24h is in good agreement with previous research [16–19]. This rapid growth confirms the destructive properties of KCl assisted HTC but gives little insight as to the mechanisms behind the accelerated corrosion. With few data-points little can be said regarding the kinetics of the corrosion.

The mass gain can be used to calculate a theoretical thickness of the oxide scale by using the density of the oxide and the weigh fraction of oxygen together with the mass gain. The calculations are based on magnetite as the only oxide formed. If $M_{Fe_2O_4} = 232$ g/mol then the weight fraction of oxygen is:

$$\frac{M_{O_2}}{M_{Fe_3O_4}} = \frac{64}{232} = 0.276 \tag{4.1}$$

The definition of density can be used to connect the mass gain per unit surface area to the thickness according to:

$$\rho = \frac{m}{V} \tag{4.2}$$

where m is the mass gain in mg/cm^2 and $\rho Fe_3O_4 = 5.17$ g/cm^3. The oxide thickness, d, is defined here as thickness on a surface area of 1 cm^2 which allows the volume to bee substituted out according to:

$$V = cm^3 = d(cm) * 1cm^2 = d \tag{4.3}$$

$$d = \frac{m}{\rho} \tag{4.4}$$

ρ in equation 4.4 is the weight fraction of oxygen multiplied by the density of the oxide which gives the final equation for the oxide thickness:

$$d = \frac{m}{\rho Fe_3O_4 * \frac{M_O2}{M_{Fe_3O_4}}} \tag{4.5}$$

In table 4.1 the theoretical thickness of oxides formed during different exposures have been calculated. This information will provide a reference for cross-sectional analysis where the actual oxide scale can be measured.

Table 4.1: Theoretical oxide thickness derived from mass gain. Values are rounded for clarity.

Sample	Surface area (cm^2)	Mass gain(mg/cm^2)	Scale thickness (µm)
1h Reference	5.4	0.02	0.1
24h Reference	5.2	0.1	0.8
168h Reference	5.3	0.3	2.1
1h KCl	5.4	0.2	1.3
24h KCl	5.4	0.9	6.3
168h KCl	5.3	1.9	13.1

4.2 Surface Analysis with SEM

An initial surface analysis was performed before exposure to determine the deposition pattern of KCl on the sample surface. A clean reference sample was also analyzed. BSE images from this analysis are presented in figure 4.2.

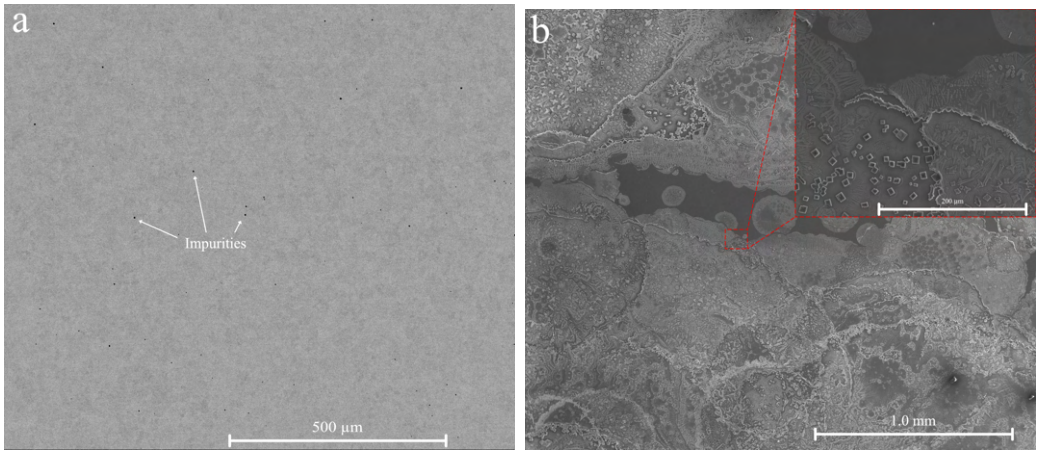

Figure 4.2: BSE images of samples before exposure. a) shows a reference sample without salt and b) shows a sample with KCl deposited.

In figure 4.2.a black spots are visible on the sample surface. These spots are also visible on the surface of exposed reference samples and in the cross-sections of all samples. EDX shows a composition containing trace amounts of aluminum and calcium, neither of which should be present in the base alloy. These spots are therefore assumed to be impurities from manufacturing. In figure 4.2.b the salt is shown to be evenly dispersed across the sample surface with a tendency to form clusters with a higher concentration of salt crystals interspersed with regions containing only trace amounts of salt.

4.2.1 Surface Analysis of Reference Samples

On all reference samples a homogenous oxide layer structured as a needle-like network had formed on the surface. No crack formation or spallation was observed on the samples. In figure 4.3 BSE images showcase the surface of reference samples after exposure.

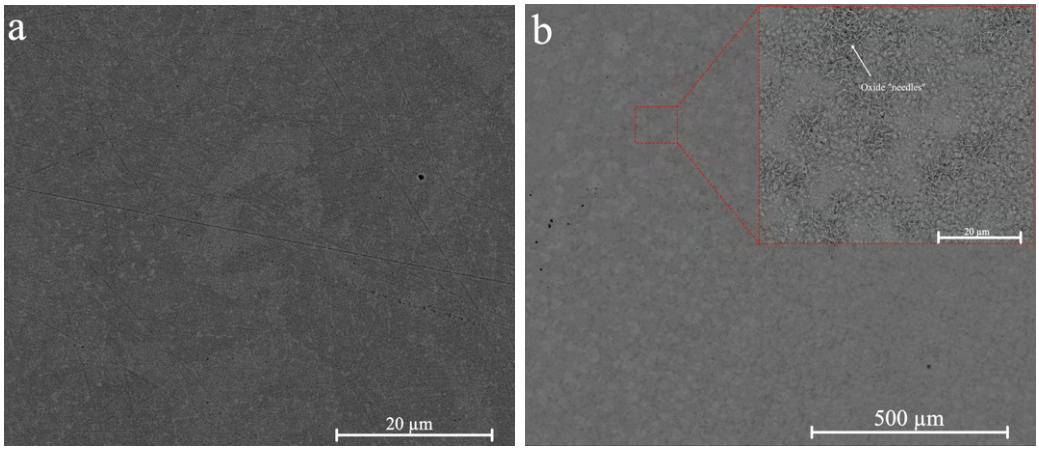

Figure 4.3: Surface images taken in BSE mode. a) shows the surface of a reference sample after 1h of exposure and b) shows the surface of a reference sample exposed for 24h

Figure 4.3.b showcases the surface of a 24h reference sample and this uniformity is representative of all reference samples. A close-up of the surface illustrates the needle-like structure of the oxide surface. In figure 4.3.a scratches from sample polishing during pre-treatment can still be seen due to a very thin oxide layer after 1h of exposure. After 24h of exposure the oxide layer was thick enough to cover these scratches completely. XRD-data confirmed the presence of both Hematite, Fe_2O_3, and Magnetite, Fe_3O_4, on samples exposed for 24- and 168h. A weak hematite/-magnetite signal was found on the 1h reference sample but most peaks were from the iron of the bulk material. Combined hematite/magnetite peaks were also visible. These peaks were difficult to evaluate due to overlap between the hematite and magnetite signals. Figure 4.4 shows XRD diffractograms for reference samples after 1,24 and 168h of exposure.

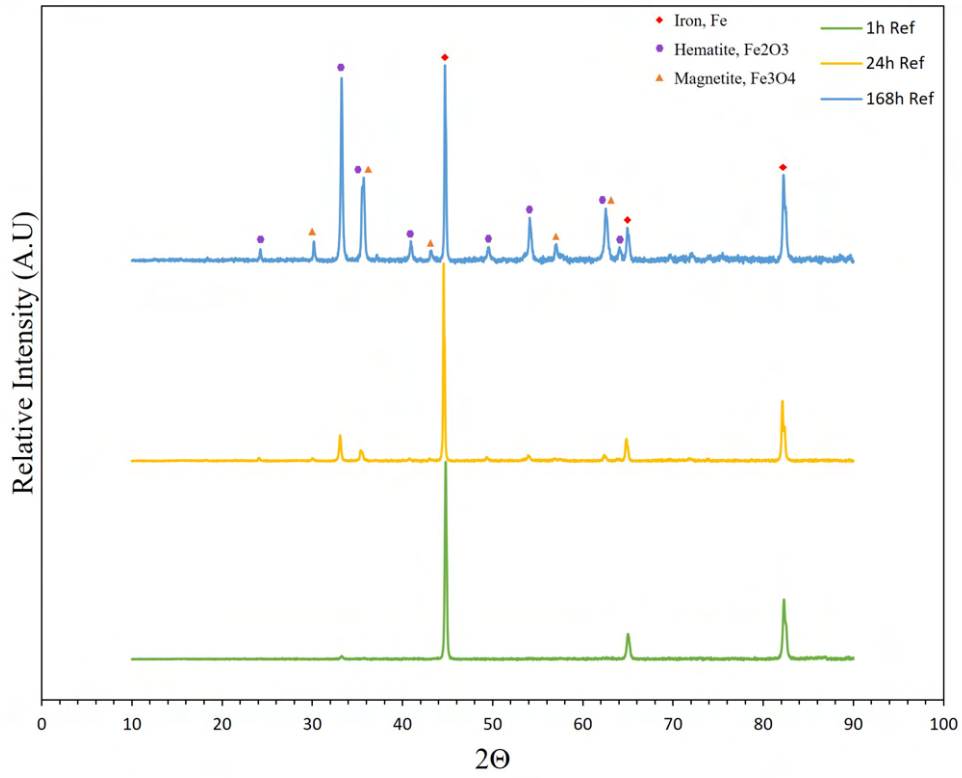

Figure 4.4: XRD data for reference samples after exposure.

The XRD data shows a weak signal from hematite after as early as 1h. Signals from both hematite and magnetite show up after 24h which makes it hard to determine the scale growth from XRD alone.

4.2.2 Surface Analysis of Samples with Deposited KCl

Samples exposed to KCl were observed to achieve a much greater variance in oxide-scale formation. A large amount of intact and semi-intact KCl particles were found on all samples with areas surrounding crystals seeing a thicker and more heterogenous oxide development. Oxide topography resembling ridges of thick, heterogenous oxide and clustered KCl particles interspersed with flatter, homogenous regions. These homogenous regions were largely free of any remaining KCl particles. Some KCl particles were discovered being actively overgrown by oxide. Signs of both cracking and spallation were visible after only 1h and after 24h and 168h excessive crack formation covered large parts of the sample surface indicating a rapid rate of corrosion. Figures 4.5 and 4.6 show overview images of samples exposed for 1h and 24h.

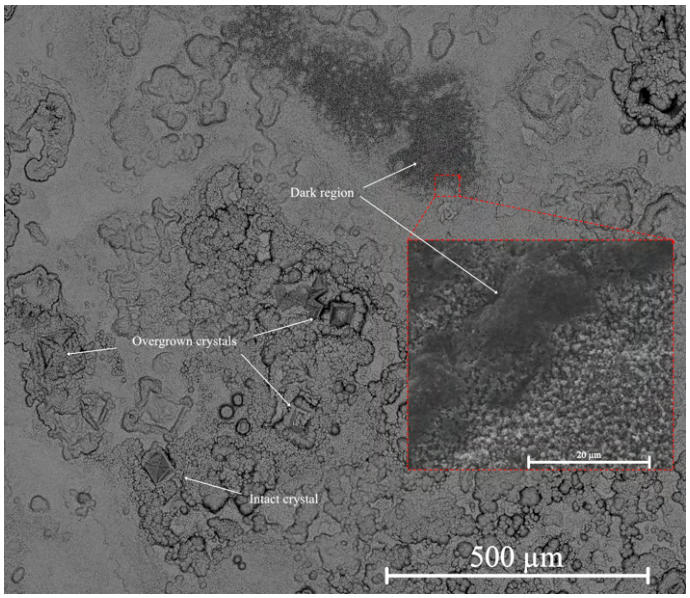

Figure 4.5: SEM images from a sample with deposited KCl after 24 hours of exposure. Highlighted are the differences in oxide topography and the different states of KCl particles found on the surface. A close up of the surface taken in SE mode shows the different microstructures of dark and light regions.

Figure 4.5 shows the surface of a sample exposed for 24h and showcases the different regions found on the surface. The visibility of intact salt crystals on the surface has drastically decreased compared to the sample exposed for 1h in figure 4.6.a as most crystals have become overgrown by the oxide-scale. Some parts of the surface consisting of more homogenous regions appear in a darker tone when viewed in BSE mode which is believed to be due to a local dense microstructure. The difference between these areas is easily discernible when observed in SE mode in the close-up of figure 4.5.

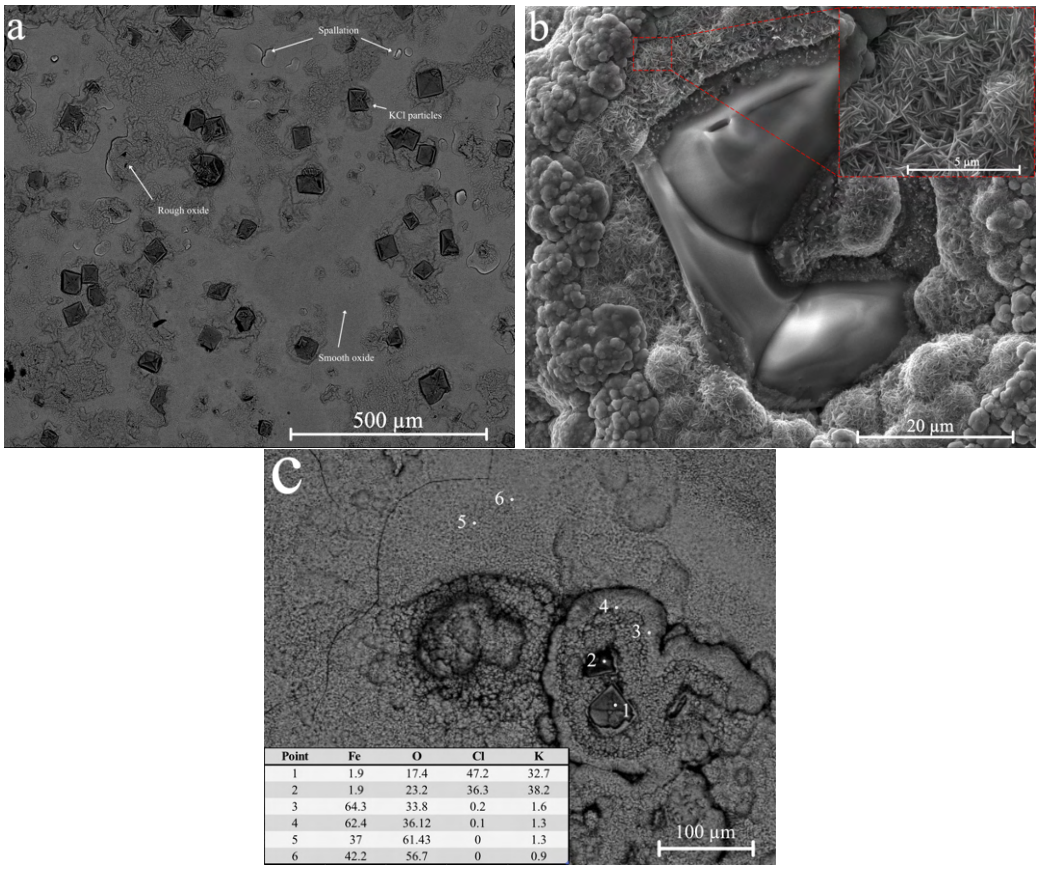

Point	Fe	O	Cl	K
1	1.9	17.4	47.2	32.7
2	1.9	23.2	36.3	38.2
3	64.3	33.8	0.2	1.6
4	62.4	36.12	0.1	1.3
5	37	61.43	0	1.3
6	42.2	56.7	0	0.9

Figure 4.6: Figure a) shows a BSE image of a sample after being exposed for 1h. b) is a SE image of a salt-crystal found on a sample after 24h and showcases the blade-like microstructure of the oxide overgrowing it. b) depicts the point-analysis done with EDX on a sample after 168h of exposure. Ratios are in atmoic %.

In figure 4.6.a The limited exposure time has left most salt particles intact on the surface but signs of aggressive oxide formation around them are appearing. Figure 4.5.b shows the microstructure found around the KCl particles. Depicted is one being overgrown by oxide which has formed in needle-like structures. A close up of the crystal in figure 4.5.b, taken in SE mode, shows the microstructure clearly. This microstructure is known to be typical for hematite [20]. Even after 168h intact salt crystals could be identified on the surface and point analysis using EDX confirmed a 1:1 atomic ratio between chlorine and potassium. Interference from the surrounding iron-oxide was also detected. Figure 4.6.c includes a table detailing the compositional information obtained from point analysis at different parts of the sruface. Point 2 clearly indicates the presence of intact KCl particles after 168h.

The excessive crack-formation along with signs of spallation can be seen on samples exposed for 168h in figure 4.7. The cracks were found to cover a majority of the sample surface as seen in figure 4.7.a. At certain points flakes (figure 4.7.b) and holes were observed in connection to crack formation. In figure 4.7.c a crack has formed through an oxide nodule on the surface. It is unknown if crack formation

ocurred during exposure or as a result of the sample cooling and the oxide-volume decreasing which can lead stress.

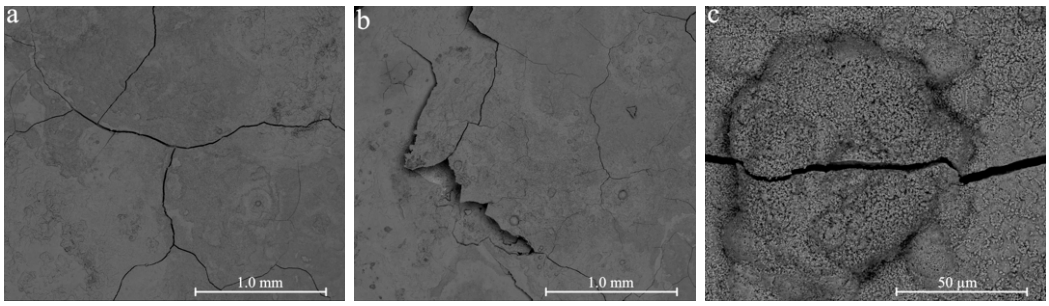

Figure 4.7: Cracking and spalling of KCl exposed samples after 168h.

XRD confirmed the presence of both hematite,Fe_2O_3, and magnetite,Fe_3O_4, which were observed in the same needle-like configuration previously seen on reference samples. XRD results from salt-exposed samples in figure 4.8 indicated a much earlier formation of both hematite, Fe_2O_3, and magnetite, Fe_3O_4 where signals from both oxides were present even after one hour of exposure. In addition to the iron oxides the mineral form of KCl, sylvite, was detected on all salt-exposed samples. This is expected since SEM images show residual salt crystals even after 168h of exposure as was also confirmed by EDX in figure 4.6.c.

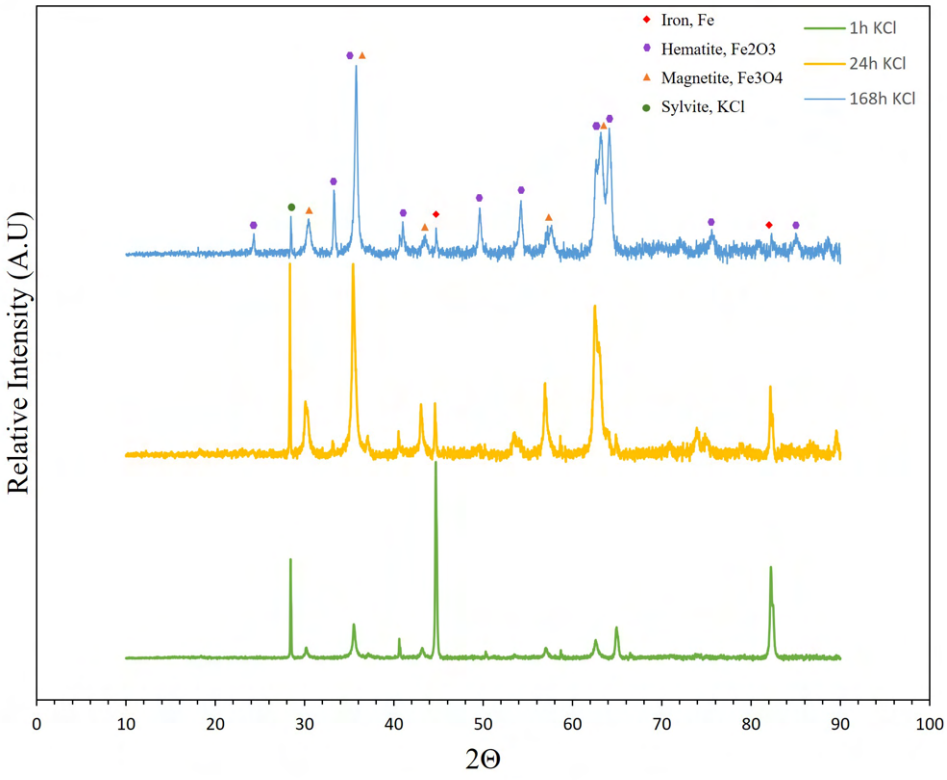

Figure 4.8: XRD data after exposure of samples deposited with KCl.

4.3 Cross-sectional Analysis with SEM

In this section cross-sectional images of selected regions are presented. For a representative view of the different cross-sections refer to figures A.1-6 in appendix A.

BSE imaging of reference sample cross-sections (figures 4.9.a-c) revealed thin, well adherent scales growing homogenously across the surface. The scale found on the 1h sample (figure 4.9.a) was very thin, approximately 0.2 µm thick which is close to the theoretical value derived from the mass gain. No large difference could be observed on reference samples after 24h (figure 4.9.b) apart from a slightly thicker scale, measuring in at approximately 1µm. Early signs of spallation were observed in some areas of the cross-section. After 168h (figure 4.9.c) the scale was easily observed on the surface with a thickness of 2.5µm. Furthermore an inward-growing oxide was observed beneath the primary oxide-scale as shown in the close-up of figure 4.9.c. EDX analysis (figure 4.10.a) indicated that the outward growing layer consisted of magnetite, Fe_3O_4, with a Fe:O atomic ratio of approximately 44:55. This, however, is unlikely due to the presence of characteristic hematite needles on the surface of the oxide. The inward-growing oxide had a lower oxygen content and a Fe:O ratio of around 53:41 which does not coincide with either magnetite or hematite formation. This might indicate a mixed oxide composition or interference from surrounding material. EDX analysis proved insufficient in determining the exact composition of the inward-growing oxide as interference from the bulk material and the outward growing oxide were likely at play. Small voids also began appearing under the oxide layer of the reference sample (figure 4.9.c) after 168h which might represent early stages of spallation. Significant spallation was not observed on reference samples even after 168h of exposure.

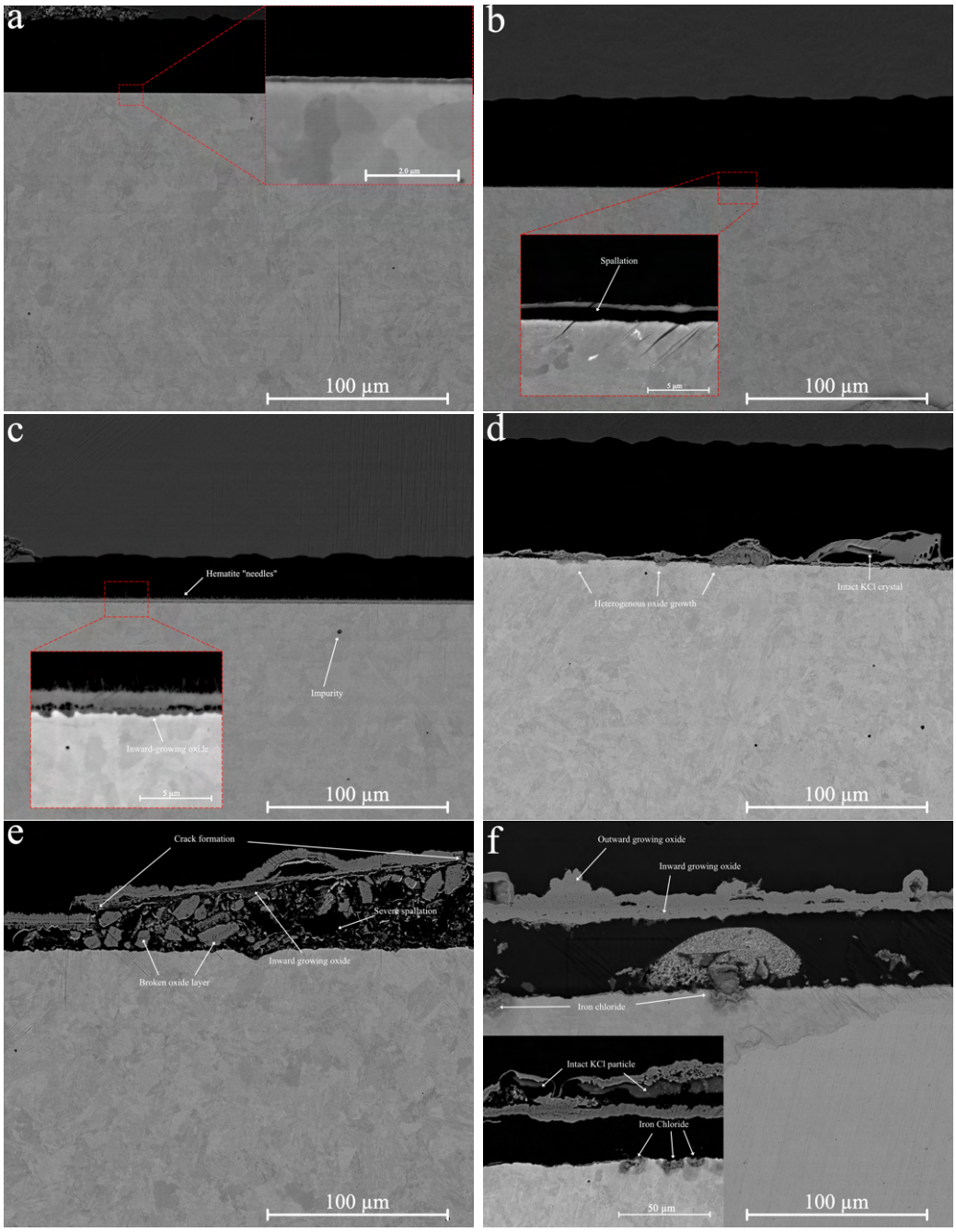

Figure 4.9: Cross-section images of reference, and salt-exposed samples. Images taken in BSE mode. a): reference after 1h, b): reference after 24h, c): reference after 168h, d): KCl sample after 1h, e): KCl sample after 24h, f): KCl sample after 168h. Selected images are representative of the majority of the cross-section.

Cross-sectional analysis of salt-exposed samples (figures 4.9.d-f) revealed a much larger variance in topography. Even after 1h (figure 4.9.d) heterogenous oxide growth can be seen as rough regions have already started to emerge. An intact KCl particle is also visible in the cross-section. After only 24h (figure 4.9.e) the oxide-scale has almost completely detached from the surface. Figure 4.9.e shows a region of

particularly aggressive spallation. Crack formation could be seen in the topmost oxide layer and an inward growing oxide was spotted adhering to the spalled-off outer layer. After 168h (figure 4.9.f) the oxide-scale had completely detached from the underlying metal leaving a void in between. The oxide-scale is made up of two clear phases. One outward-growing phase and one inward-growing. As seen in figure 4.10.d EDX revealed the presence of chlorine believed to be in the form of iron-chloride along the base alloy interface across the entirety of the surface. KCl particles, largely intact, were also observed buried beneath the oxide scale in another region of the scale shown in figure 4.9.f and were quantified using EDX (figure 4.10.d).

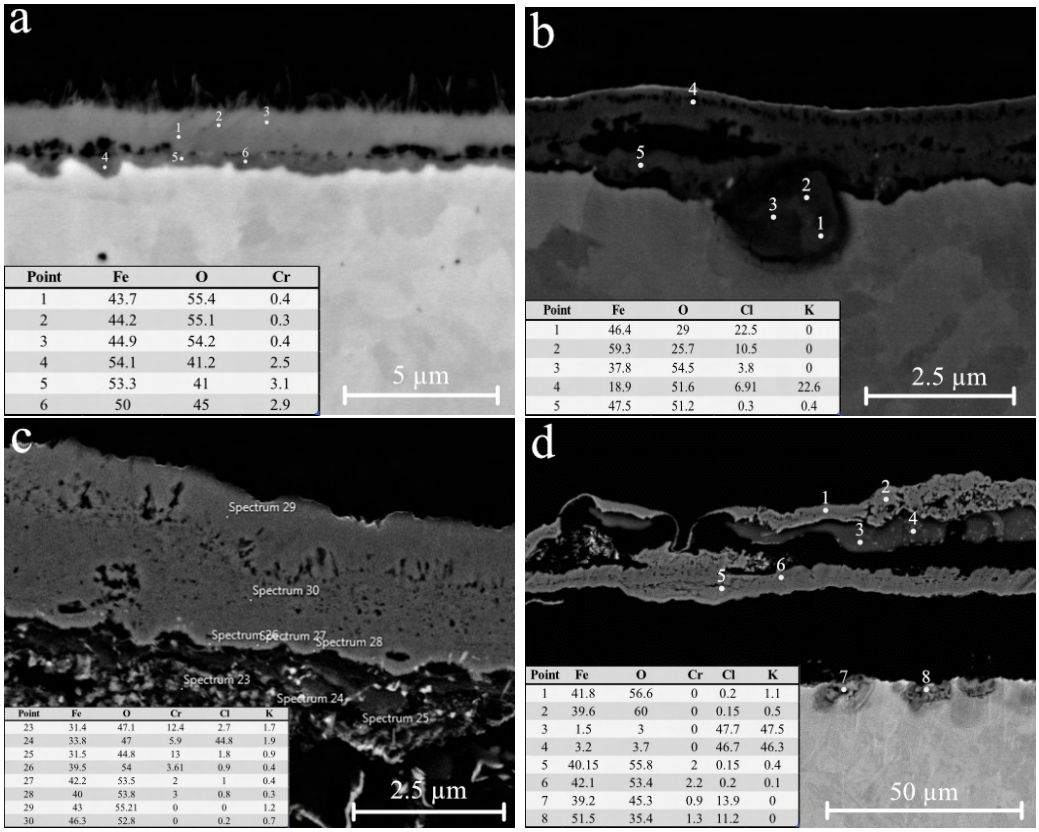

Point	Fe	O	Cr
1	43.7	55.4	0.4
2	44.2	55.1	0.3
3	44.9	54.2	0.4
4	54.1	41.2	2.5
5	53.3	41	3.1
6	50	45	2.9

Point	Fe	O	Cl	K
1	46.4	29	22.5	0
2	59.3	25.7	10.5	0
3	37.8	54.5	3.8	0
4	18.9	51.6	6.91	22.6
5	47.5	51.2	0.3	0.4

Point	Fe	O	Cr	Cl	K
23	31.4	47.1	12.4	2.7	1.7
24	33.8	47	5.9	44.8	1.9
25	31.5	44.8	13	1.8	0.9
26	39.5	54	3.61	0.9	0.4
27	42.2	53.5	2	1	0.4
28	40	53.8	3	0.8	0.3
29	43	55.21	0	0	1.2
30	46.3	52.8	0	0.2	0.7

Point	Fe	O	Cr	Cl	K
1	41.8	56.6	0	0.2	1.1
2	39.6	60	0	0.15	0.5
3	1.5	3	0	47.7	47.5
4	3.2	3.7	0	46.7	46.3
5	40.15	55.8	2	0.15	0.4
6	42.1	53.4	2.2	0.2	0.1
7	39.2	45.3	0.9	13.9	0
8	51.5	35.4	1.3	11.2	0

Figure 4.10: EDX point analysis performed on cross-sections of: a) 168h reference sample, b) 1h KCl sample, c) 24h KCl sample and d) 168h KCl sample. Cross sections of reference samples after 1h and 24h are not represented here due to them adding little information of value. With the exception of chromium alloying elements are of little interest and have been left out. All results displayed in atomic %.

Figure 4.10 contains compositional information obtained using EDX point-analysis of different samples. Reference samples exposede for 1h and 24h are not represented here due to their uniform thin growth leading to little of interest separating them from the reference sample after 168h.

4.3.1 Compositional Maps of Cross-Sections using EDX

In this section cross-sectional analysis of KCl-exposed samples using EDX will be presented to investigate whether or not the proposed chlorine-cycle mechanism is valid for low-alloyed steels. As mentioned in section 2.1.5 an indication that would strengthen this theory is the existence of chlorine beneath the oxide-scale as this would indicate metal-chloride formation has occured.

Upon investigating the cross-section of a sample exposed for 1h (figure 4.11.a) the only chlorine detected seemed to be that of a intact KCl particle on the sample surface. However, a closer view (figure 4.11.b) revealed the presence of a chlorine-containing particle under the oxide-scale in the absence of potassium. Point analysis confirmed the presence of both iron and chlorine in varying concentrations but this result was not considered very accurate due to substantial interference from the surrounding material. No inward oxidation was observed after 1h.

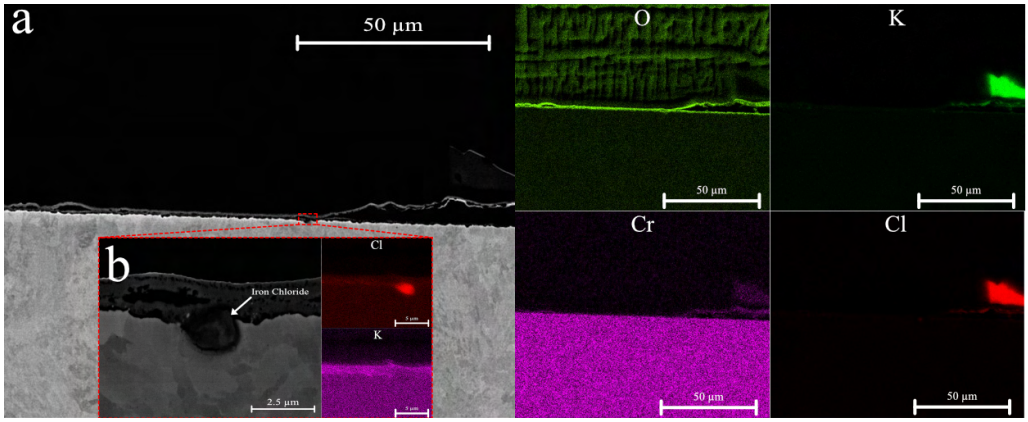

Figure 4.11: BSE cross-section of a KCl sample after 1h of exposure with added EDX maps. a) shows a zoomed out cross-section and b) a zoomed-in view of a chlorine-rich zone found under the oxide scale.

During EDX analysis of 24h samples (figure 4.12) heavy spallation was observed over most of the surface. Contrasts between the outward growing scale and a inward growing one were clearly visible as seen in section 4.3 even after spallation of both phases. EDX mapping suggested a Cr-enriched inward growing scale which was confirmed with point-analysis (figure 4.10.c). Point-analysis of the inward-growing scale of other samples (figure 4.10.a and 4.10.d) did not show a significantly higher Cr-content than the bulk material but this could be due to a lower degree of magnification. Again, point-analysis was not considered very accurate and interference likely gave a misrepresentative view of the scale composition. Crack formation was also observed through the oxide-scale at several locations (figure 4.12.b). Once again chlorine was found underneath the scale but traces of potassium were also present indicating the possibility of KCl particles making their way through the oxide through the cracks in the outer scale.

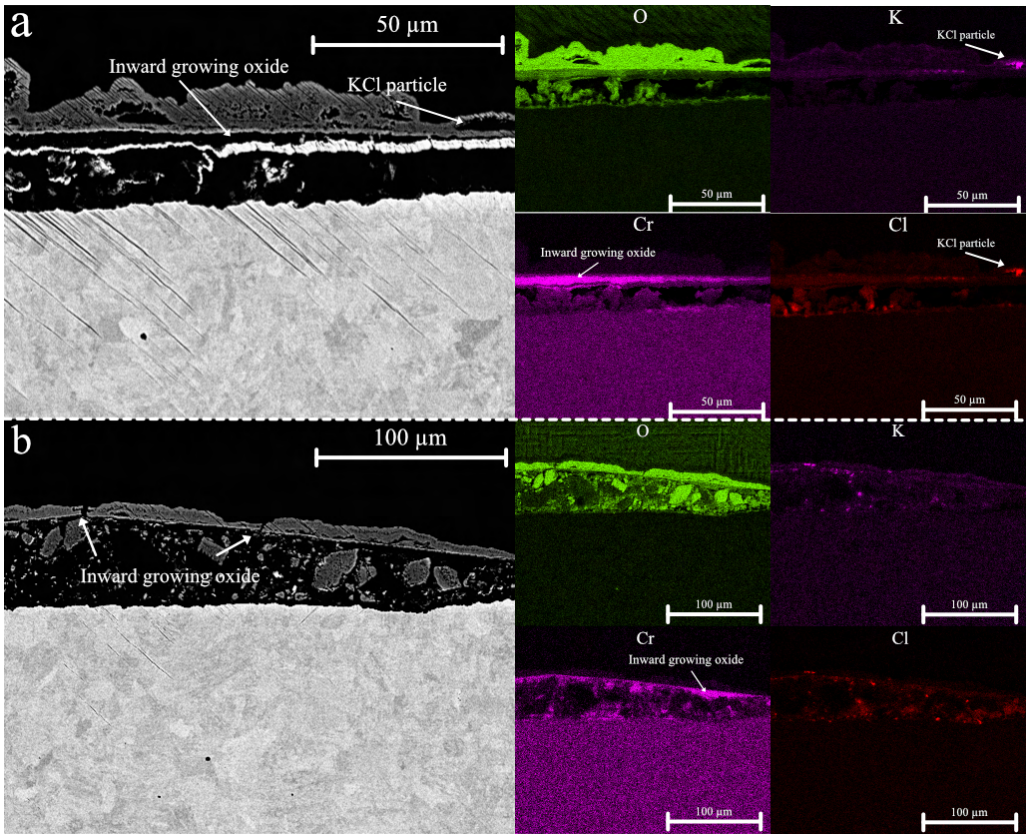

Figure 4.12: BSE cross-section of a KCl sample after 24h of exposure with added EDX maps. a) and b) illustrate different regions of the same sample. Significant spallation is seen in both regions along with a Cr-enriched inward-growing oxide.

As was observed from SEM images after 168h (figure 4.13) the scale had completely detached from the sample surface. In consistence with samples after 24h the oxide layer appeared to be composed of two different phases. One outward-growing and one inward-growing with the inward-growing one showing an increased content of chromium. Chlorine was more prevalent beneath the scale than it had been in previous samples with evenly spaced out particles found along the alloy interface (figure 4.13.a-b). The clear decoupling of chlorine from potassium strongly indicates it is able to diffuse down, through the scale, to the metal/oxide interface. Intact KCl particles were also detected underneath the topmost layer of the scale (figure 4.13.b).

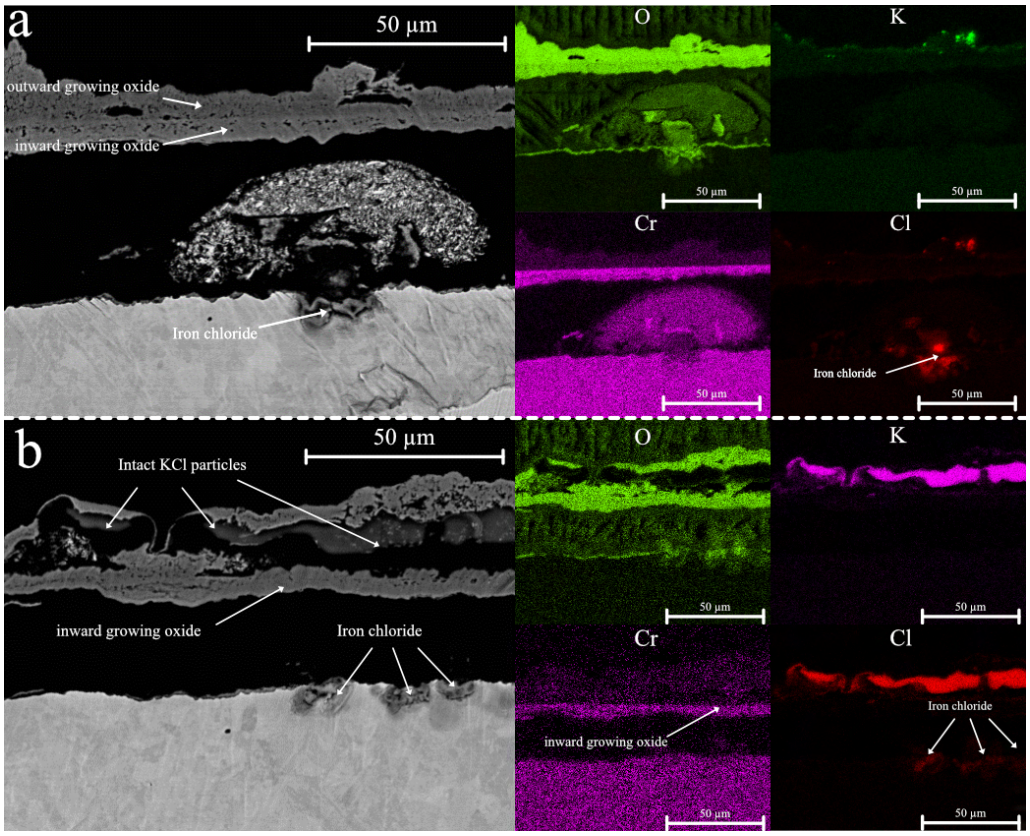

Figure 4.13: BSE cross-section of a KCl sample after 168h of exposure with added EDX maps. a) and b) illustrate different regions of the same sample. Chlorine-rich regions under the oxide-scale are prevalent after 168h

5 | Conclusion

The aim of this report was to investigate the nature of a KCl-induced high-temperature corrosion attack on low-alloyed steels and to determine whether previously proposed mechanisms of corrosion were reasonable in the working conditions used. This investigation was undertaken using SEM analysis to investigate both topography and cross-sections of samples with- and without deposited KCl. XRD was used to determine which phases of oxide where present on the sample surface and EDX was used in an attempt to quantify the oxide composition. As discussed in sections 2.1.5.1-2. the proposed chlorine-cycle, or electrochemical corrosion mechanisms are both characterised by the formation of metal-chlorides on the metal-oxide interface. As such, finding evidence of the formation of these chlorides was of great interest.

Mass gain data was too limited to provide information regarding kinetics but provided a good indicator for the severity of corrosion with KCl present. Furthermore, mass-gain data for samples exposed for 24h were compared to that of earlier research and was found to be in good agreement with reported findings [16–19]. A theoretical thickness was calculated using mass gain data and compared to the thickness measured from cross-sectional imaging. Measured values were largely consistent with theoretical ones.

XRD analysis confirmed the presence of both magnetite and hematite on every sample apart from reference samples after 1h where mostly iron and a small peak of hematite was detected. On salt-exposed samples KCl was also detected using EDX even after 168h. This was confirmed using EDX.

On reference samples after 168h and on salt-exposed samples after 24h the oxide-scale was observed to consist of two major phases. One inward-growing and one outward-growing. On reference samples after 168h hematite-needles were observed on the outward-growing scale. EDX mapping indicated an enrichment of chromium in the inward-growing scale altough point-analysis using EDX did not show any meaningful concentration compared to the bulk material for most samples. Quantification of the oxide-scale composition proved difficult as no clear match could be made to either hematite or magnetite when point-analyzing different parts of the scale. This is believed to be due to interference from the bulk material and the surrounding oxide.

EDX mapping of KCl-exposed samples revealed the presence of chlorine beneath the scale surface. Chlorine was found clearly detached from potassium strongly indicating chlorine is able to migrate through the oxide-scale and reach the alloy interface. Point-analysis of these spots revealed a composition high in both iron and chlorine indicating the possibility of iron-chloride formation. As previously stated EDX quantification of the particles was taken with a grain of salt due to interference from the bulk material and as such the formation of a specific iron-chloride, $FeCl_2$, could not be confirmed. The proposed chlorine-cycle mechanism involves the dissolution of the metal-chlorides due to a high volatility. It is possible that this volatility creates a high pressure underneath the oxide-scale which could explain the severe spallation seen on most samples.

Accurately investigating the microstructure of the oxide-scale and determine the presence of different phases i.e hematite and magnetite proved difficult with the instrumentation used in the project. Using a instrument such as TEM could provide more precise information regarding the microstructure and morphology of the scale. This has been attempted by Persdotter et al. [19] and allowed for a more accurate quantification of the scale morphology.

The underlying purpose of the report was to investigate corrosion of low-alloyed steels as a result of exposure to a complex flue-gas released during the combustion of biomass in combined heat-and-power plants. Exposures to KCl alone is far from a realistic representation of the actual working conditions the steels are exposed to. For future research it could therefore be interesting to investigate exposures using a mixed composition of alkali-chlorides like KCl, HCl and $PbCl_2$ as detailed by Erik Larsson [17]. Combinations of different alkali-chlorides are shown to drastically alter the corrosion of exposed steels and gives a better picture of real-world conditions. HCl in particular is of great interest to study since the relative amount found in flue gas is much greater [17].

Bibliography

[1] Ericsson K, Werner S. The Introduction and Expansion of Biomass Use in Swedish District Heating Systems. Biomass and bioenergy. 2016;94:57-65.

[2] Jones JM, Lea-Langton AR, Ma L, Pourkashanian M, Williams A. Pollutants Generated by the Combustion of Solid Biomass Fuels. vol. 1. Springer London; 2014.

[3] Sharma S, Sharma M, Mudgal D, Bhowmick H. Adoption of strategies for clean combustion of biomass in boilers. Corrosion Reviews. 2021;39(5):387-408. Available from: https://doi.org/10.1515/corrrev-2020-0095 [cited 2022-05-11].

[4] Nielsen HP, Frandsen FJ, Dam-Johansen K, Baxter LL. The implications of chlorine-associated corrosion on the operation of biomass-fired boilers. Progress in Energy and Combustion Science. 2000;26(3):283-98. Available from: https://www.sciencedirect.com/science/article/pii/S0360128500000034.

[5] Galanopoulos C, Yan J, Li H, Liu L. Impacts of acidic gas components on combustion of contaminated biomass fuels. Biomass and Bioenergy. 2018;111:263-77. Available from: https://www.sciencedirect.com/science/article/pii/S0961953417301381.

[6] Vainikka P, Bankiewicz D, Frantsi A, Silvennoinen J, Hannula J, Yrjas P, et al. High temperature corrosion of boiler waterwalls induced by chlorides and bromides. Part 1: Occurrence of the corrosive ash forming elements in a fluidised bed boiler co-firing solid recovered fuel. Fuel. 2011;90(5):2055-63. Available from: https://www.sciencedirect.com/science/article/pii/S0016236111000226.

[7] McCafferty E. Introduction to Corrosion Science. vol. 1. New York, NY: Springer; 2010.

[8] A C Sequeira C. High Temperature Corrosion: Fundamentals and Engineering. vol. 1. John Wiley and Sons, Ltd; 2018.

[9] Young DJ. High Temperature Oxidation and Corrosion of Metals. vol. 2. Elsevier; 2016.

[10] DerSilberspiegel. Ellingham Diagram. Wikimedia Commons; 2016. Available from: https://commons.wikimedia.org/wiki/File:Ellingham_Richardson-diagram_english.svg.

[11] Olivas Ogaz MA. High Temperature Corrosion of Low-Alloyed and Stainless Steels: Mechanistic Study of Chlorine-Induced Corrosion. Chalmers University of Technology, Sweden; 2019. Available from: https://www.proquest.com/docview/2300291087.

[12] Olivas-Ogaz MA, Eklund J, Persdotter A, Sattari M, Liske J, Svensson JE, et al. The Influence of Oxide-Scale Microstructure on KCl(s)-Induced Corrosion of Low-Alloyed Steel at 400°C. Oxidation of Metals. 2019 Apr;91(3):291-310. Available from: https://doi.org/10.1007/s11085-018-9881-2.

[13] Jonsson T, Folkeson N, Svensson JE, Johansson LG, Halvarsson M. An ESEM in situ investigation of initial stages of the KCl induced high temperature corrosion of a Fe–2.25Cr–1Mo steel at 400°C. Corrosion Science. 2011;53(6):2233-46. Available from: https://www.sciencedirect.com/science/article/pii/S0010938X11001478.

[14] Folkeson N, Jonsson T, Halvarsson M, Johansson LG, Svensson JE. The influence of small amounts of KCl(s) on the high temperature corrosion of a Fe-2.25Cr-1Mo steel at 400 and 500°C. Materials and Corrosion. 2011;62(7):606-15. Available from: https://onlinelibrary.wiley.com/doi/abs/10.1002/maco.201005942.

[15] Ma HT, Zhou CH, Wang L. High Temperature Corrosion of Pure Fe, Cr and Fe–Cr Binary Alloys in O2 Containing KCl Vapour at 750°C. Corrosion Science. 2009;51(8):1861-7. Available from: https://www.sciencedirect.com/science/article/pii/S0010938X09001978.

[16] Larsson E, Liske J, Persdotter A, Jonsson T, Svensson JE, Johansson LG. The Influence of KCl and HCl on the High-Temperature Oxidation of a Fe-2.25Cr-1Mo Steel at 400°C. Oxidation of Metals. 2020 Feb;93(1):29-52. Available from: https://doi.org/10.1007/s11085-019-09943-9.

[17] Larsson E. The Corrosive Effect of Chlorine Containing Species on Waterwalls and Superheater Materials in Waste and Biomass-fired Power Plants; 2017. Available from: https://publications.lib.chalmers.se/records/fulltext/246773/246773.pdf.

[18] Larsson E, Gruber H, Hellström K, Jonsson T, Liske J, Svensson JE. A comparative study of the initial corrosion of KCl and PbCl2 on a low-alloyed steel.

Oxidation of metals. 2017;87(5):779-87.

[19] Persdotter A, Sattari M, Larsson E, Ogaz MO, Liske J, Jonsson T. Oxidation of Fe-2.25 Cr-1Mo in presence of KCl (s) at 400 C–Crack formation and its influence on oxidation kinetics. Corrosion Science. 2020;163:108234.

[20] Folkeson N, Jonsson T, Halvarsson M, Johansson LG, Svensson JE. The influence of small amounts of KCl (s) on the high temperature corrosion of a Fe-2.25 Cr-1Mo steel at 400 and 500° C. Materials and Corrosion. 2011;62(7):606-15.

[21] Uusitalo M, Vuoristo P, Mäntylä T. High temperature corrosion of coatings and boiler steels in oxidizing chlorine-containing atmosphere. Materials Science and Engineering: A. 2003;346(1-2):168-77.

[22] Ul-Hamid A. A Beginners' Guide to Scanning Electron Microscopy. vol. 1. Springer Cham; 2018.

[23] Russ JC. Fundamentals of Energy Dispersive X-ray Analysis. vol. 1; 1984.

[24] Stanjek W H Häusler. Basics of X-ray Diffraction. Hyperfine Interactions. 2004;154:107–119.

[25] Jiang R, Li M, Yao Y, Guan J, Lu H. Application of BIB Polishing Technology in Cross-section Preparation of Porous, Layered and Powder Materials: A Review. Frontiers of Materials Science. 2019;13(2):107-25.

A | Appendix 1

A.1 Cross-section overviews

A.1.1 Reference sample overviews

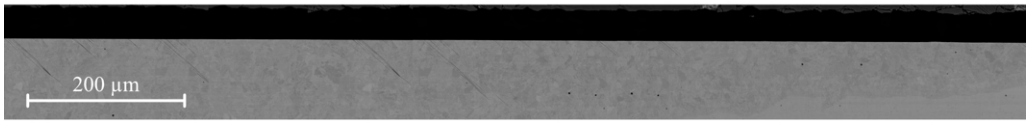

Figure A.1: Representative view of a reference sample cross-section after 1h.

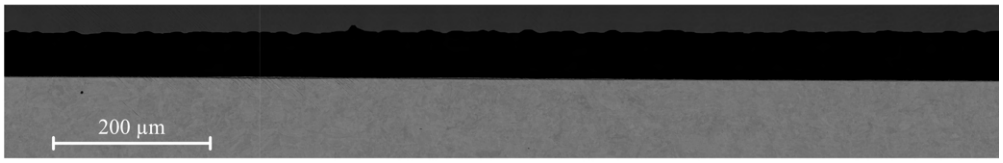

Figure A.2: Representative view of a reference sample cross-section after 24h.

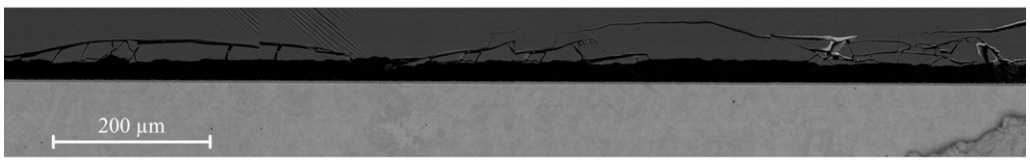

Figure A.3: Representative view of a reference sample cross-section after 168h.

A.1.2 KCl sample overviews

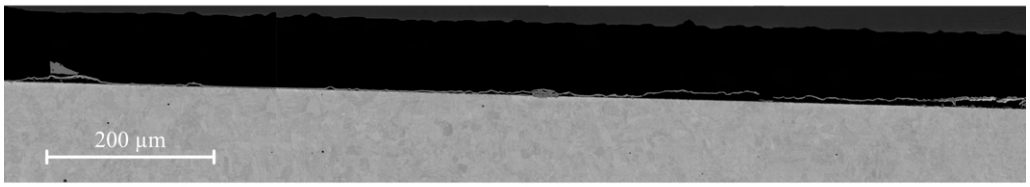

Figure A.4: Representative view of a salt-exposed sample cross-section after 1h.

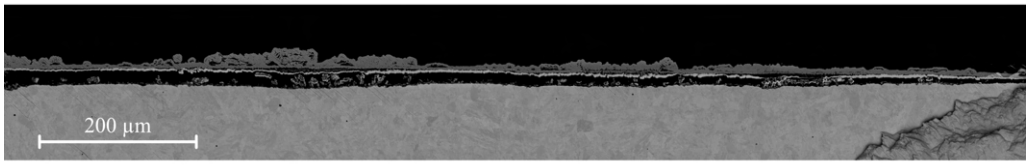

Figure A.5: Representative view of a salt-exposed sample cross-section after 24h.

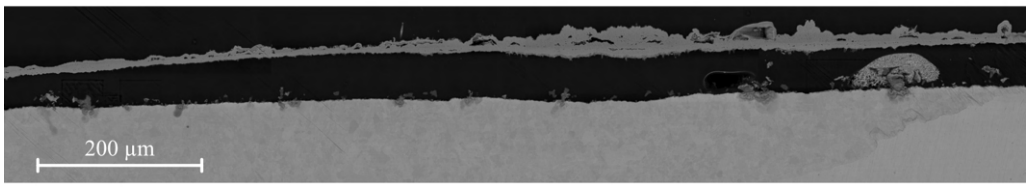

Figure A.6: Representative view of a salt-exposed sample cross-section after 168h.

DEPARTMENT OF CHEMISTRY AND CHEMICAL ENGINEERING
CHALMERS UNIVERSITY OF TECHNOLOGY
Gothenburg, Sweden, 2022
www.chalmers.se

CHALMERS